Lawrence Berkeley National Laboratory
LBL Publications

Title
In-situ density and litho-constrained modeling of gravity data in the Los Humeros geothermal field, Mexico

Permalink
https://escholarship.org/uc/item/75b5r6jc

Journal
Geothermal Energy, 14(1)

ISSN
2195-9706

Authors
Cornejo-Triviño, Natalia
Leandra, M
Weydt
et al.

Publication Date
2026-12-01

DOI
10.1186/s40517-026-00395-4

Copyright Information
This work is made available under the terms of a Creative Commons Attribution License, available at https://creativecommons.org/licenses/by/4.0/

Peer reviewed

eScholarship.org Powered by the California Digital Library
University of California

Cornejo-Triviño *et al. Geothermal Energy* (2026) 14:19
https://doi.org/10.1186/s40517-026-00395-4

Geothermal Energy

RESEARCH Open Access

In-situ density and litho-constrained modeling of gravity data in the Los Humeros geothermal field, Mexico

Natalia Cornejo-Triviño[1], M. Leandra[1], Weydt[1], Ingo Sass[1,2] and Eva Schill[3*]

*Correspondence:
Eva Schill
eschill@lbl.gov
[1]Institute of Applied Geosciences, Technical University of Darmstadt, Darmstadt, Germany
[2]Geoenergy, GFZ – Helmholtz Centre for Geoscience, Potsdam, Germany
[3]Lawrence Berkeley National Laboratory, Berkeley, CA, USA

Abstract

To improve the reliability of gravity-based geothermal reservoir characterization, this study evaluates density parameterization strategies for constraining gravity modeling and inversion in the complex volcanic setting of the Los Humeros Geothermal Field (LHGF), Mexico. We integrate gravity data, a 3-D geological model, and petrophysical measurements to evaluate three density parameterizations in the starting models: (C1) mean bulk density, (C2) compaction-corrected saturated bulk density, and (C3) a multimodal density distribution derived from lithologic sub-volumes.
Forward modeling results show a consistently poor fit on the order of several mGal between observed and computed gravity data across all three parameterizations, characterized by a persistent negative bias in the computed gravity and only limited improvement despite optimized initial densities. Inverse modeling that accounts for compaction effects and saturated-porosity densities significantly reduces the misfit between observed and computed gravity, generally to below 1 mGal. A detailed misfit analysis reveals that our initial density values consistently underestimated optimal densities by 60–130 kg/m^3. The misfit shows no systematic variation with depth but seems to be linked to lithology. The low salinity of reservoir fluids (≤ 4 g/L) suggests that salinity effects are negligible. The multi-modal density approach (C3) does not improve the fit and introduced skewness, likely due to volumetric estimates of lithologies derived from limited available data for the individual units.
Inversion tests with varying probabilities of density and geometry changes revealed that for the LHGF a 70:30 ratio produced the most optimal model, confirming the overall consistency of the initial 3-D geological model with observed gravity data. Smaller density variations in pre-caldera units suggest greater homogeneity, while fault zones likely contribute to localized heterogeneity in the underlying units.
Our results do not distinguish between the conventional and superheated sectors of the LHGF, highlighting that gravity anomalies in this volcanic system primarily reflect the geological structure rather than thermal or fluid characteristics. Finally, our methodology provides a practical framework for quantifying uncertainty of 3-D geological models.

© The Author(s) 2026. **Open Access** This article is licensed under a Creative Commons Attribution 4.0 International License, which permits use, sharing, adaptation, distribution and reproduction in any medium or format, as long as you give appropriate credit to the original author(s) and the source, provide a link to the Creative Commons licence, and indicate if changes were made. The images or other third party material in this article are included in the article's Creative Commons licence, unless indicated otherwise in a credit line to the material. If material is not included in the article's Creative Commons licence and your intended use is not permitted by statutory regulation or exceeds the permitted use, you will need to obtain permission directly from the copyright holder. To view a copy of this licence, visit http://creativecommons.org/licenses/by/4.0/.

Introduction

Besides revealing the geological structure of the subsurface, gravity anomalies in geothermal fields have been associated with temperature anomalies (Baillieux et al. 2013) and attributed to fracture porosity that facilitates the circulation of thermal fluids (Altwegg et al. 2015; Baillieux et al. 2014; Guglielmetti et al. 2013). However, as a potential field method, gravity surveys of the subsurface yield non-unique solutions for density distributions (Telford et al. 1990). To reduce this inherent uncertainty, models are often constrained using additional and independent data.

In volcanic geothermal environments, Witter et al. (2016) performed 3-D inversion modeling of gravity data in the Bradys geothermal area (Nevada, USA), using a 3-D geological model to constrain the inversion and applying both homogeneous and heterogeneous starting density values. However, at the time of the study, a comprehensive database of rock density values covering the area was unavailable, and the starting densities were not validated with field measurements. In other studies, where petrophysical data from rock samples are available, mean density values are often used as starting parameters. Yet, these values typically neglect the volumetric proportions of different lithologies within each model unit and are not corrected for in-situ reservoir conditions (e.g., Guillen et al. 2008). Given that density is sensitive to saturation and compaction changes and considering the inherent heterogeneity of geothermal reservoirs relying on mean or estimated densities can introduce significant uncertainties and obscure local variations in gravity data that may be critical for accurate reservoir characterization.

This study aims to identify the most effective parameterization method for inverse modeling of gravity data in heterogeneous volcanic geothermal reservoirs. Specifically, we investigate the influence of saturated porosity and compaction on input parameters used for forward modeling and inversion of gravimetric data. Our approach integrates gravity data, a 3-D geological model, and petrophysical analyses, and is applied to the Los Humeros Geothermal Field (LHGF). At LHGF, most geological units consist of multiple lithologies with distinct rock properties (Calcagno et al. 2022; Weydt et al. 2021), providing an ideal setting to evaluate progressively refined starting models, culminating in a multi-modal density distribution, for forward and inverse modeling.

We proceed by testing both the in-situ density and the lithology-constrained initial densities. We compare the results of inverse modeling using three different density parameterizations per geological model unit: (1) a single mean density; (2) a single mean saturated porosity density corrected for compaction effects; and (3) a multi-modal density distribution incorporating saturated porosity and compaction corrections. The third approach accounts for the volumetric fraction of individual lithologies within each geological unit, considering both thermal and overburden conditions. Additionally, we explore different probabilistic approaches for altering model parameters at lithological boundaries and for adjusting density values.

Geological setting

The LHGF, Mexico's third-largest geothermal field, is situated in the northeastern part of the Trans-Mexican Volcanic Belt (TMBV, see inset map in Fig. 1). It is predominantly composed of Pleistocene to Holocene basaltic to rhyolitic lavas. The basement underneath the LHGF consists of Mesozoic sedimentary rocks of the Sierra Madre Oriental, which are characterized by prominent NW–SE-striking thrusts and folds, along with

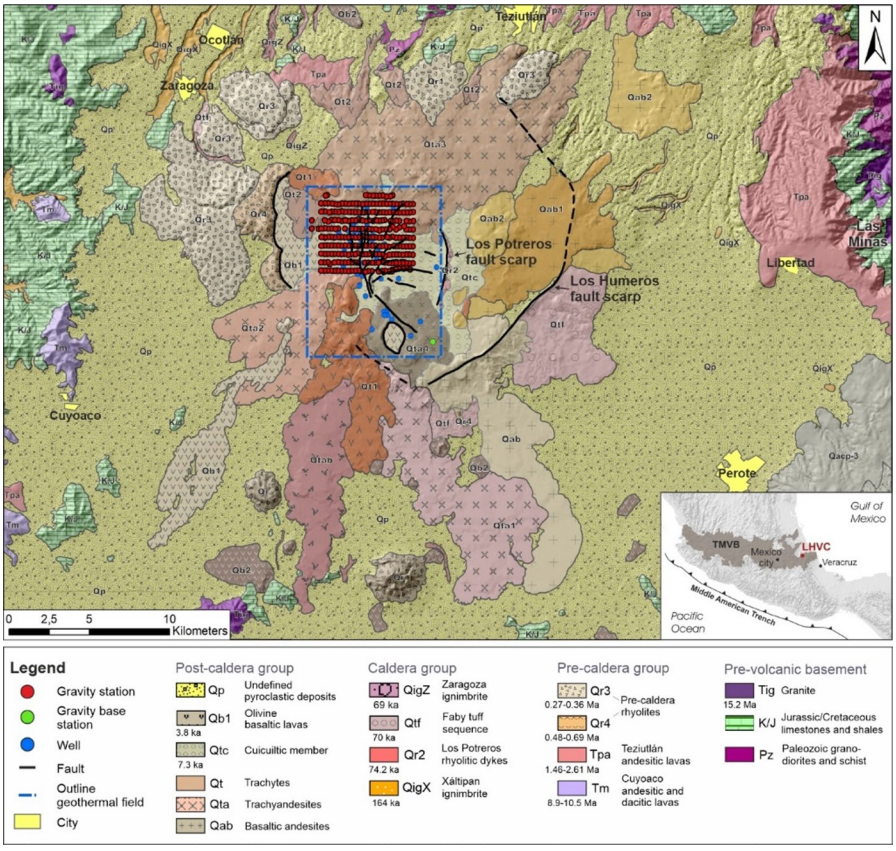


Fig. 1 Geologic map of the Los Humeros Volcanic Complex (LHVC; modified from Carrasco-Núñez et al. 2017a). Inset map showing the location of the LHVC and extension of the Trans-Mexican Volcanic Belt (TMVB). Red dots mark the gravity stations within the Los Humeros caldera covering the central to northern part of the geothermal field

secondary NE-striking normal faults (Norini et al. 2019). The basement rocks have been locally metamorphosed to marble, hornfels and skarn near dykes as well as syenitic to granitic plutons that intruded into the sedimentary sequences (Yáñez-García and García-Durán 1982).

The volcanic succession in the study area is classified into three groups: pre-caldera, caldera, and post-caldera (Figs. 1 and 2b). The pre-caldera group, with a thickness of up to approximately 1,500 m, is primarily composed of extensive basaltic, basaltic andesitic, and andesitic lavas of the Teziutlán Formation, 2.6–1.4 Ma (Carrasco-Núñez et al. 2022) as well as locally older basaltic lavas and lavas of the Cuyoaco Formation (8.9–10.5 Ma). Furthermore, the pre-caldera group includes basaltic to rhyolitic lavas and lava domes (270–693 ka; Carrasco-Núñez et al. 2018) at approximately 1000 m below ground level with a variable thickness and limited extension, which represent the onset of magmatic activity of the Los Humeros Volcanic Complex. These pre-caldera lavas, particularly the Teziutlán Formation, represent the currently exploited, predominantly fracture-controlled reservoir of the LHGF, which were affected by multiple hydrothermal alteration events, leading to locally increased matrix porosities (Weydt et al. 2022b).

The Xáltipan ignimbrite, 164 ka (Carrasco-Núñez et al. 2018) is a thick pyroclastic unit that is associated with the formation of the main Los Humeros caldera. Its thickness ranges from 90 to 780 m and porosity can reach up to 70% when part of the reservoir

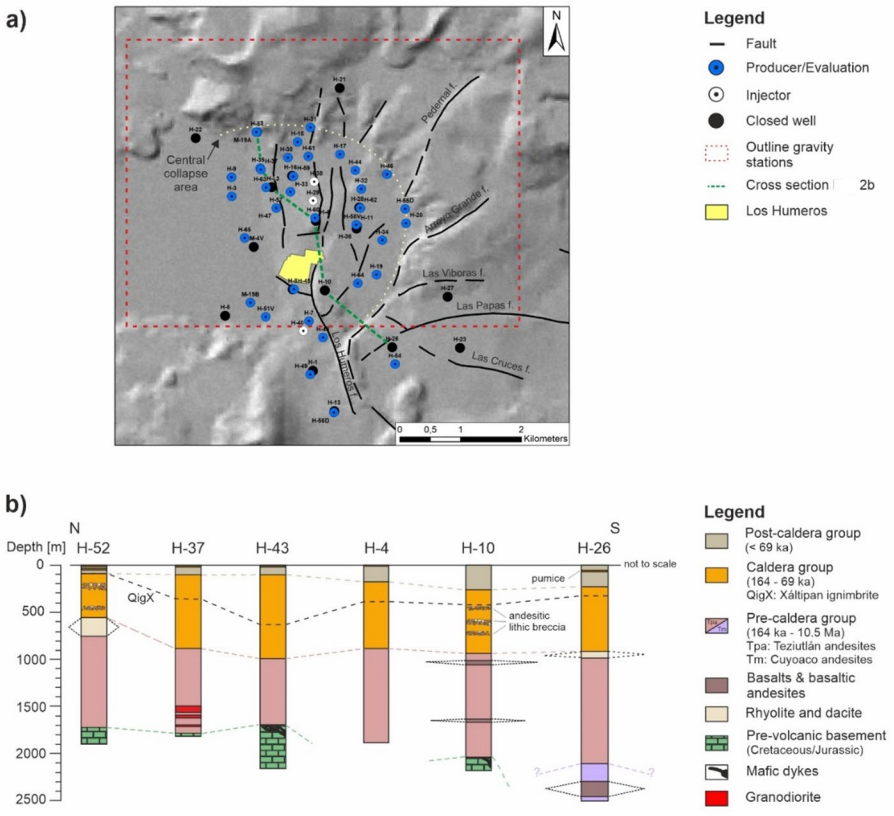


Fig. 2 (**a**) Location of the geothermal wells of the LHGF modified from Carrasco-Núñez et al. (2017a). (**b**) Simplified lithostratigraphic profiles and in-depth correlation of the main stratigraphic groups modified from Weydt et al. (2022b) and based on Urbani et al. (2021); Carrasco-Núñez et al. 2017b); Cavazos-Álvarez et al. (2020). Post-caldera group: U1, and U2; Caldera group: U3, U4 and U5; Pre-caldera group: U6, U7, and U8 in (Calcagno et al. 2022) geological model

volume (Cavazos-Álvarez et al. 2020; Weydt et al. 2022a). Overlying the Xáltipan ignimbrite is the Faby Tuff, 70 ka (Ferriz and Mahood 1984; Willcox 2012). The second caldera-forming event corresponds to the emplacement of the Zaragoza ignimbrite 2–60 m thick, 69 ka (Carrasco-Núñez et al. 2012, 2018), which led to the formation of the smaller Los Potreros caldera (8–10 km in diameter), nested within the Los Humeros caldera.

The post-caldera group encompasses a Late Pleistocene resurgence phase, marked by rhyolitic to dacitic lavas and pyroclastic deposits, followed by a Holocene reactivation phase characterized by widespread explosive and effusive volcanism. Due to the high geological complexity—featuring variable lithologies, thicknesses, and extents—this group displays complex rock properties (Weydt et al. 2022a, b).

The geothermal fluid in the LHGF is characterized by high temperatures exceeding 300 °C in the deeper, superheated zones (Prol-Ledesma and Browne 1989). It has very low salinity with total dissolved solids typically around 1 g/L and rarely exceeding 4 g/L (Bernard et al. 2011; Tello 2005), making its chemical composition like that of dilute meteoric water. The fluid is primarily of meteoric origin, with minimal magmatic input (Pinti et al. 2021), and exists under both liquid-dominated and superheated vapor-dominated conditions depending on depth and reservoir location.

Materials and methods

Geological model of the LHGF and its surroundings

The LHGF is situated in the western section of the Los Humeros caldera, with its eastern boundary marked by the Los Potreros fault scarp. The distribution of geothermal producers and injectors (about 40 wells in total) is shown in Fig. 2a. Along a NNW-SSE transect through the LHGF, Fig. 2b presents lithostratigraphic profiles for selected wells.

To compare with the density models derived from our measurements, we use the local 3-D geological model proposed by Calcagno et al. (2022). This model includes nine geological units and 21 modeled faults (Fig. 3; Table 1). The model extends across a volume of 9.5 km by 12.5 km horizontally, and 12 km vertically (with 7 km below sea level).

Acquisition of gravity data

Gravity data were collected in the central to northern regions of the LHGF (Cornejo-Triviño et al. 2024). The survey consists of 263 gravity stations along ten east-west profiles, each 5.5 km in length, with typical station spacing of 200 m and profile separation of 500 m. Measurements were acquired in November-December 2017 using a CG-5 Autograv Gravity Meter (Scintrex Ltd.), with an instrumental accuracy of one micro-Gal. At each gravity station, a mean value from three 120-second measurements was calculated. The locations of the gravity stations were determined by differential GPS (DGPS) using two Trimble 5700 receivers and two Trimble antennas (TRM39105 and TRM41249), with a vertical accuracy of 5 mm. Out of the 263 measurements, two were discarded due to unreliable DGPS records.

The standard deviation of the gravity measurements, corrected for thermal and leveling effects, ranges from 0.008 to 0.119 mGal. For the DGPS measurements, the range is between 0.0012 and 0.3893 m. Applying thresholds of 0.05 mGal for gravity and 0.2 m for DGPS results in 247 stations selected for further processing and modeling to investigate the distribution of densities in the LHGF.

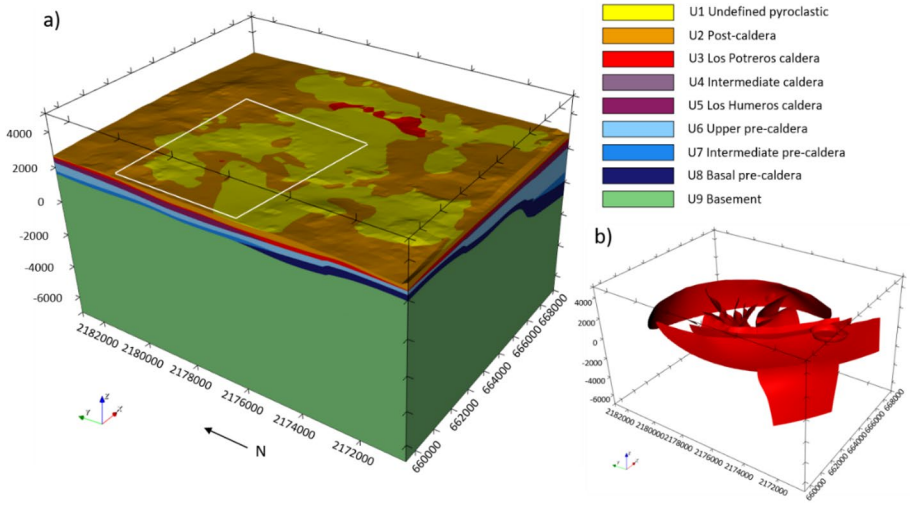


Fig. 3 **a**) Local 3-D geological model of the LHGF (Calcagno et al. 2022) with the white square indicating the area used for gravity modeling. **b**) Modeled faults. Vertical exaggeration: 0.7

Table 1 Overview of the input densities of the geological model units 1–9 for the three applied cases C1-3

Model Unit	C1 Mean bulk density [kg m^{-3}]	C2 Compaction corrected and saturated mean bulk density [kg m^{-3}]	C3		
			Lithology	Compaction corrected and saturated mean bulk density [kg m^{-3}]	Volume estimation [%]
U1 Undefined pyroclastic	1,480	1,890	Undefined pyroclastic deposits	1,890	100
U2 Post-caldera	2,090	2,117	Rhyodacite (4%), tuff (4%), and pumice (17%); weighted mean value	1,500	25
			Andesitic lava	2,600	25
			Basaltic lava	2,420	50
U3 Los Potreros caldera	1,600	1,905	Andesitic lava	2,600	36
			Tuff	1,930	60
			Pumice	1,200	4
U4 Intermediate caldera*	1,530**	2,260	Tuff	1,930***	50
			Andesitic lava	2,590***	50
U5 Los Humeros caldera	1,450	2,212	Upper Xáltipan ignimbrite (not to slightly welded)	1,880	35
			Middle Xáltipan ignimbrite (slightly to moderately welded)	2,310	50
			Basal Xáltipan ignimbrite (highly welded)	2,450	15
U6 Upper pre-caldera	**2,490**	**2,425**	**Rhyolitic lavas**	**2,450**	**20**
			Basaltic to andesitic lavas	**2,400**	**80**
U7 Intermediate pre-caldera	**2,320**	**2,550**	**Basaltic to andesitic lavas**	**2,440**	**40**
			Basaltic to andesitic lavas (low porosity)	**2,660**	**60**
U8 Basal pre-caldera	**2,500**	**2,615**	**Basaltic to andesitic lavas**	**2,440**	**70**
			Skarn	**2,800**	**30**
U9 Basement	2,750	2,798	Marble	2,680	85
			Granite	2,620	10
			Skarn	3,100	5

C1: mean bulk densities from Weydt et al. (2021), C2: saturated mean bulk densities values corrected for fluid pressure and temperature (P/T) and compaction at depth, C3: saturated mean bulk densities values corrected for fluid P/T and compaction at depth and accounting for the main lithologies for the individual unit. Units of the pre-caldera group U6 to U8 include the geothermal reservoir rocks marked in bold

* = no outcrops or wellbore core data available, **=average value was calculated from U3 and U5, ***= estimations based on data from U3

Data processing

To estimate the instrumental drift, daily repeated gravity measurements were conducted at a base station located 8 km from the survey area (Fig. 1, green dot) to monitor instrumental drift. Earth tide, instrumental drift, latitude, and elevation corrections were calculated using GravProcess software (Cattin et al. 2015). The instrumental drift correction was estimated by a least-squares fit of the weighted time series at this station with a first-order polynomial function. Earth tidal effects were corrected for each gravity measurement following the methods outlined by Agnew (2007, 2012). Free-air and simple Bouguer corrections were made using the DGPS-processed data.

The topographic correction was performed using Oasis Montaj software (Seequent) using the algorithms formulated by Kane (1962) and Nagy (1966) and digital elevation models (DEMs) with progressively decreasing resolution, extending up to a maximum distance of 166.7 km from each gravity measurement (LaFehr, 1991). The DEMs used in the calculations included a 1 m-resolution DEM (Centro Mexicano de Innovacion en Energía Geotérmica, CeMIEGeo) covering most of the gravity measurement area, and a 15 m-resolution DEM (Instituto Nacional de Estadística y Geografía, INEGI), which was resampled to a lower resolution as the distance from the stations increase:

a. From 1 m at the station to 10 m,
b. To 15 m from 10 m to 1 km,
c. To a reduced cell size of 50 m from 1 km to 10 km,
d. To a reduced cell size of 500 m from 10 km to 100 km, and.
e. A reduced cell size of 5 km from 100 km to 167 km.

A density of 2,670 kg m^{-3} was used to calculate the simple and complete Bouguer anomaly (CBA). Considering the standard deviation threshold of the DGPS measurements, the uncertainty introduced by the terrain correction is estimated to be less than 0.06 mGal. The uncertainty in elevation introduced from the DEM is approximately 0.6 mGal. When combined with the standard deviation threshold of the gravity measurements (0.05 mGal), the total mean uncertainty is about 0.7 mGal.

To estimate the regional trend, a Gaussian filter was applied to a CBA incorporating 13,737 measurements from the Comisión Nacional de Hidrocarburos (Cornejo-Triviño et al. 2024). The resulting residual anomaly is referred to as the "observed gravity" in subsequent analyses.

Forward and inverse modeling

In this study, the 3-D local geological model of the LHGF (Calcagno et al. 2022) was used to constrain both the forward and inverse gravity modeling. The geological model, discretized into a voxel grid with a cell size of 200 m in the XY direction and 100 m in the Z direction down to 0 m a.s.l., consists of 17,388 voxels (nx = 28; ny = 23; nz = 27). The observed gravity data were sampled according to the acquisition frequency along the profiles, with oversampling between profiles to maintain a regular 2-D grid resolution of 200 m × 200 m.

Forward and inverse modeling calculations were carried out using GeoModeller software (Intrepid Geophysics), which computes the gravimetric forward response based on the equations of Plouff (1976), Okabe (1979), and Holstein (2003). The inverse modeling utilizes a Markov Chain Monte Carlo Stochastic Inversion method, as described in Calcagno et al. (2008) Guillen et al. (2008). This method systematically adjusts both the geological model and starting densities based on a given probability of change. Various probabilities for modifying densities and lithology boundaries were tested to assess confidence in the geological model and density estimates.

The geometry of the model was controlled through three geological constraints implemented in GeoModeller, which are the parameters often used to geologically constrain a stochastic inversion:

1. Commonality test, the number of voxels in common between the proposed models and the reference model is controlled statistically using a commonality constraint.

Commonality constraint is typically controlled with a Weibull distribution with shape = 1 (therefore exponential). We adopted a scale parameter of 0.20, corresponding to a moderate constraint (~ 80% overlap with the starting model).

2. Shape Ratio test, the ratio between the shape of the current model and the shape of the reference model. A shape ratio constraint will aim to preserve the shape of a lithology. A shape ratio constraint will have the side effect of limiting the change in volume of a lithology and neighboring lithologies. It is controlled with a log-normal distribution. We used a spread measure (standard deviation) of 0.10, representing a moderate constraint.
3. Preserve Vertical Relationships (PVR), which maintains the stratigraphic order of units.

To ensure that each cell of the discretized geological model (17,388 voxels) was perturbed at least 10 times during the inversion process, the total number of iterations was set to 173,880. This number of perturbations guarantees a thorough exploration of the parameter space and enhances the reliability of the results. Conversion of observed and calculated data is achieved by reducing the least square deviation.

Our analysis is based on the misfits between observed and calculated gravity using Eq. 1.

$$\delta_{g,misfit} = \delta_{g,observed} - \delta_{g,computed} \tag{1}$$

with δ_g = gravity. Positive/negative misfits reveal an underestimation/overestimation of the gravity in the model. The histograms of the misfit are evaluated using the standard deviation and kurtosis, a statistical measure of the "tailedness" of a distribution. A high kurtosis indicates a distribution with heavier tails than a normal distribution, meaning there are more outliers or extreme values.

1.1 Model parameterization and density optimization

To assess the impact of saturated porosity and compaction on the input data for forward modeling and inversion of gravimetric data, we performed forward modeling using three density parametrizations (case 1 to 3):

C1: one mean bulk density value per geological unit,
C2: one mean saturated bulk density value per geological unit that is corrected for compaction at depth, and
C3: a multi-model saturated bulk density distribution that accounts for the density of individual lithologies within each geological unit.

For C1, the values were derived from laboratory measurements on dry core samples from the geothermal field or dry outcrop analogues of its surrounding areas (Weydt et al. 2021). Note that, due to a lack of samples, the density value for model unit U4 is represented by the mean of the values from units U3 and U5. To account for the full range of modeling possibilities, we additionally performed density optimizations for case C1. The algorithm utilizes a bounded least-squares approach to refine the density estimates, constraining the optimization within ± 2 times the density standard deviation (100 kg m^{-3}).

The saturated mean bulk density for C2 and C3 was calculated using Eq. (2). C2 consider one mean saturated bulk density per geological unit and for C3, we assigned up to

three different lithologies to each lithostratigraphic unit, with a standard deviation of 100 kg m^{-3} and a normal distribution for the density values.

$$\rho_{\mathrm{Bsat}} = \phi \cdot \rho_{\mathrm{F}} + (1 - \phi) \cdot \rho_{\mathrm{M}} \tag{2}$$

with ρ_{Bsat} = bulk density at depth, ρ_{F} = fluid density for the temperature and pressure conditions at depth, ρ_{M} = matrix density of the rock, and ϕ = porosity at depth. The depth and thickness of the lithostratigraphic units were obtained from Calcagno et al. (2022) and revised lithological borehole profiles from Carrasco-Núñez et al. (2017b); Cavazos-Álvarez et al. (2020). Changes in porosity with depth to account for compaction were calculated following Ashena et al. (2020), based on Athy (1930), using Eq. (3)

$$\phi = \phi_0 e^{-cf*z} \tag{3}$$

where ϕ_0 is the porosity measured in the laboratory, cf is the formation compaction calculated for each individual unit based on P-wave and S-wave velocities (Weydt et al. 2022a), and z is the depth. Although Athy's empirical relationship was originally developed for sedimentary rocks, it is widely used today and is derived from borehole log data. However, due to the lack of well-log information, in our study cf values were calculated following the approach presented in Ashena et al. (2020), based on P- and S-wave velocities. This approach allowed defining realistic cf values for each unit and approximating porosity-depth trends in both volcanic and sedimentary lithologies, despite the lack of well-log. Note that temperature-dependency of density in rocks is only a few percent at temperatures > 400 °C (Zhu et al. 2022) and is therefore not considered here.

The input densities for the three cases C1-3 are provided in Table 1.

Results

Observed gravity in the LHGF

The gravity data obtained in the LHGF exhibits a clear decreasing trend from WSW to ENE (Fig. 4a). This trend disrupts the regional NE-SW trending negative gravity anomalies (Fig. 4b) that were attributed to deep-rooted fault zone which feed the geothermal system (Cornejo-Triviño et al. 2024). The elevated gravity values in the WSW region coincide spatially with the rim of the Los Humeros caldera, whereas the gravity low in the ENE links to the younger deposits in the caldera.

Forward modeling

In Fig. 5, we compare the forward-modeled gravimetric responses (computed gravity, Fig. 5a-d) derived from the 3-D geological model using the initial densities for three cases C1-3. Our analysis is based on the respective misfit values between the observed (Fig. 4a) and computed gravity (Fig. 5a-d). Cases C1, both with and without optimization, and C2 capture the spatial distribution of the observed anomalies, albeit with a significant shift toward negative values. While the observed anomalies range from – 12 to 2 mGal (Fig. 4a), the computed gravity dynamics span from – 50/-31 to -30/-16 mGal (Figs. 5a-c). The misfit histograms reveal a trend from left skewed towards more Gaussian distribution from C1 to C2 (Figs. 5i-k), but much of the misfit highlights a significant underestimation of gravity in the forward models. Although the misfit for C3 shifts to lower values in more cells (Fig. 5l), it remains relatively high.

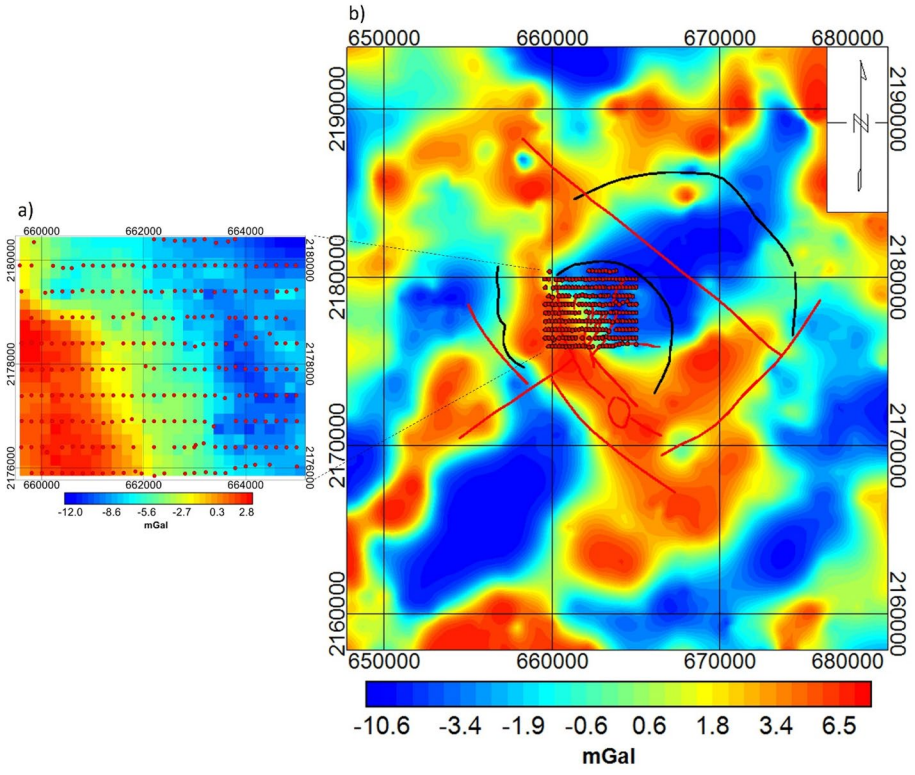


Fig. 4 **a**) Local residual gravity anomaly of the LHGF **b**) Regional residual anomaly of the Los Humeros caldera and surroundings (Cornejo-Triviño et al. 2024). Red dots indicate the locations of the gravity stations

Inverse modeling

In Fig. 6, we compare the observed gravity measurements with the gravity response after perturbing each cell 10 times using the 3-D geological models and input densities for the three cases (C1, C2, and C3). During the inversion process, both the geological model and the densities are allowed to change with an equal probability of 50%. A significant improvement in the misfit between the observed and calculated gravity is achieved in C2. At its half-width, the Gaussian distribution shows a variation of ± 0.2 mGal. When applying the multi-modal approach, the misfit distribution shifts toward more negative values.

To achieve convergence and a Gaussian distribution of the misfit using the multimodal approach, we increased the number of iterations perturbing each cell 40 times instead of 10 times (Fig. 7). This increase resulted in a half-width of 0.2 mGal.

In the following analysis, we assess the relative confidence in the initial density distribution and structural model of the inversion after perturbing each cell 40 times using C2 as the starting model, allowing for changes in their probability (Table 2). We begin by performing tests in 20% increments, first allowing changes only in density (with a 100% probability of property change for the structural model) to finally allowing changes only in the structural model (with a 0% probability of property change for density). The best fit is displayed using the standard deviation.

A relatively good overall fit, with a standard deviation of < 0.3 mGal, is observed in four of the seven realizations. The lowest standard deviation occurs in the realization with a 60% probability of property changes for density and 40% for the structural model (Fig. 8a). Although the kurtosis is highest among the realizations with standard

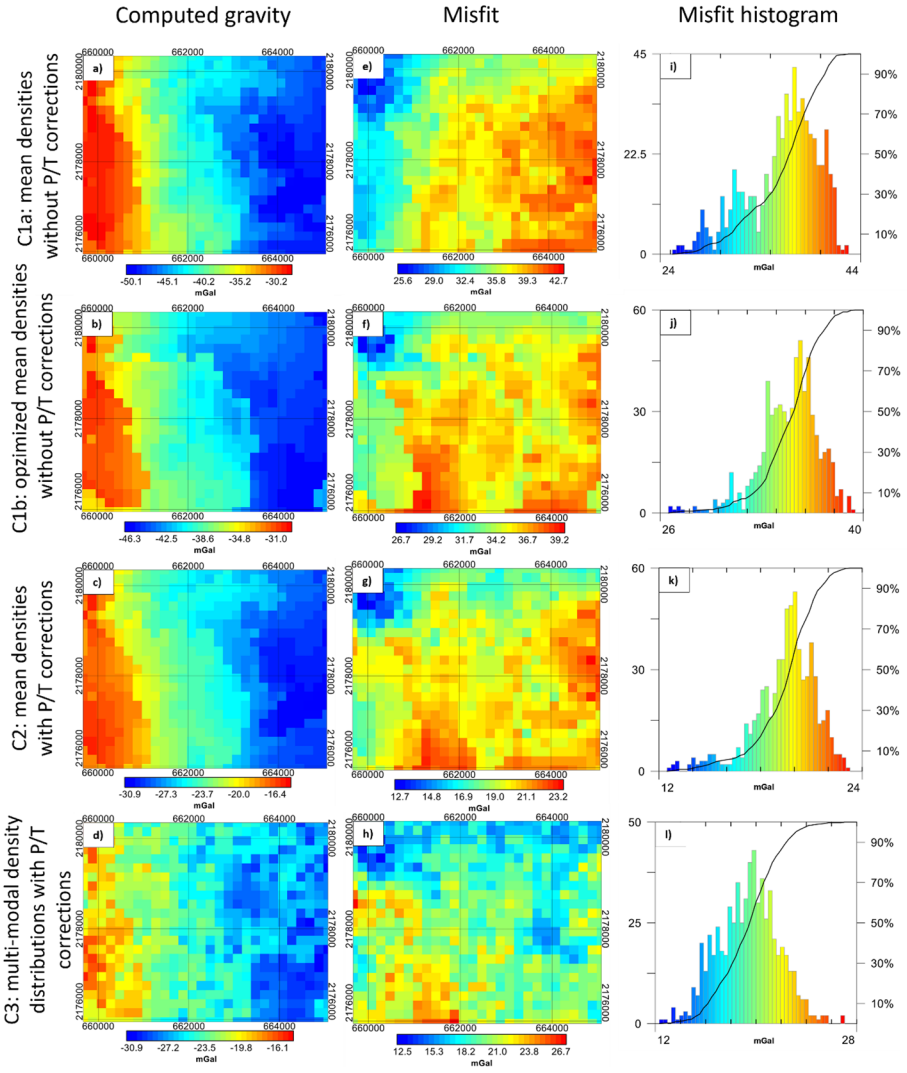


Fig. 5 Forward modeled of gravity data in the LHGF using the geological model of Calcagno et al. (2022) as a starting model with input density values of **a**) and **b**) C1, **c**) C2 and d) C3. C1b includes density optimization. **e**) to **h**) shows the respective misfits in a map view, while **i**) to **l**) shows the misfit in histograms

deviations < 0.3 mGal, the realization with an 80% probability for density changes and 20% for the structural model also exhibits the highest skewness (Fig. 8b). The additional realization with a 70% probability for density changes and 30% for the structural model reveals the lowest overall standard deviation, along with low kurtosis and relatively low skewness (Fig. 8c). In conclusion, the analysis suggests that the best fit is achieved by prioritizing density changes over structural model adjustments.

In Fig. 9, we present the 3-D density distribution of the LHGF derived from inverse modeling using the 3-D geological model from Calcagno et al. (2022) with the density distribution C2. The probability of density and structural changes were set to 70% and 30%, respectively. We would like to emphasize here that our final model reveals columns of higher density along the fault zones. This coincides with relatively large misfits along major fault zones in Fig. 6e.

The histograms of the density distributions in representative model units are presented in Fig. 10, while the complete set of units (U1-U9) is provided in the Supplementary

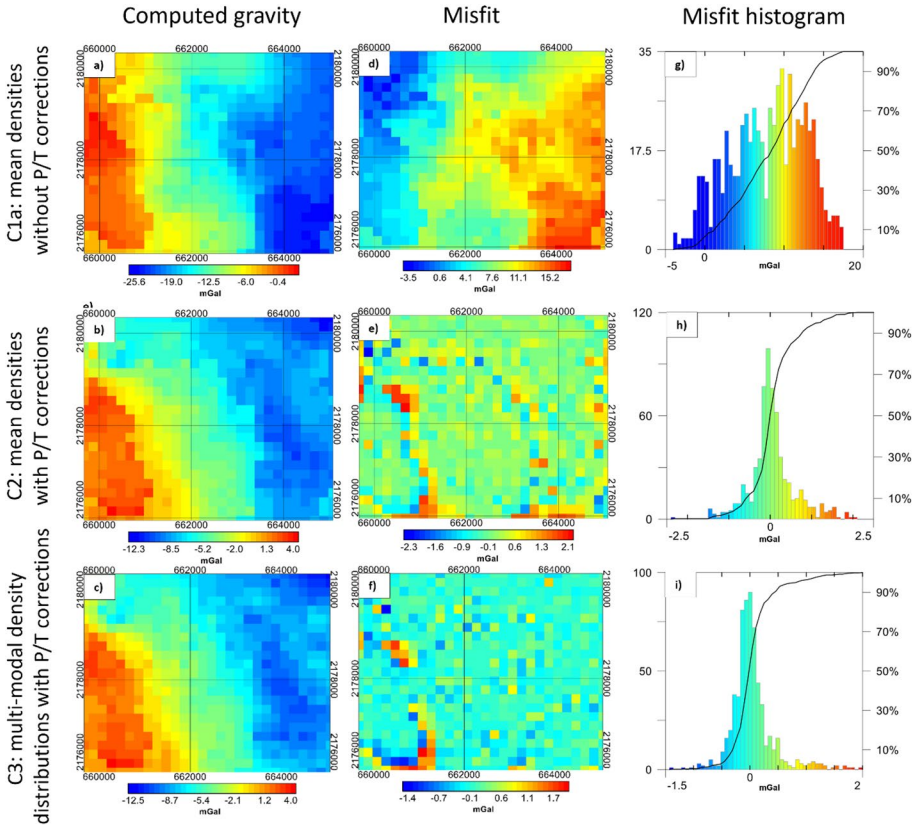


Fig. 6 Inversion of gravity data in the LHGF using the geological model of Calcagno et al. (2022) as a starting model with input density values of **a**) C1a, **b**) C2 and **c**) C3. **d**) to **f**) shows the respective misfits in a map view, and **g**) to **i**) shows the misfit in histograms. The computed gravity data are displayed after perturbing each cell 10 times

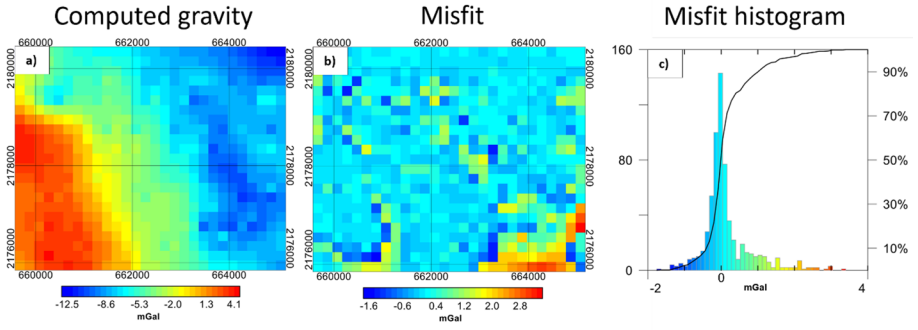


Fig. 7 Inversion of gravity data in the LHGF using the geological model of Calcagno et al. (2022) as a starting model with input density values of C3. **a**) shows the computed gravity, **b**) shows the misfit between computed and observed gravity in a map view, and **c**) shows the misfit histogram. The computed gravity data are displayed after perturbing each cell 40 times

Material (Supplementary Figs. 1–9). Although the applied corrections for compaction and fluid saturation in C2, our input saturated mean bulk densities were consistently underestimated by approximately 60–130 kg/m^3. Analysis of the individual geological units shows a clear trend toward log-normal density distributions from Unit 1 to Unit 5, indicating decreasing variability and asymmetry in rock properties (see Supplementary

Table 2 Probabilities of density and/or geometry changes and their corresponding misfits between observed and calculated gravity for C2 after perturbing each cell 40 times

Probability of property change		Overall standard deviation (mGal)	Kurtosis (mGal)	Skewness
Density (%)	Structural model (%)			
100	0	0.577	2.286	1.323
80	20	0.294	6.113	1.192
70	30	0.273	4.945	0.851
60	40	0.273	5.087	0.937
50	50	0.292	5.711	0.951
40	60	0.289	5.990	0.994
20	80	0.337	4.686	0.535
0	100	0.871	1.292	0.425

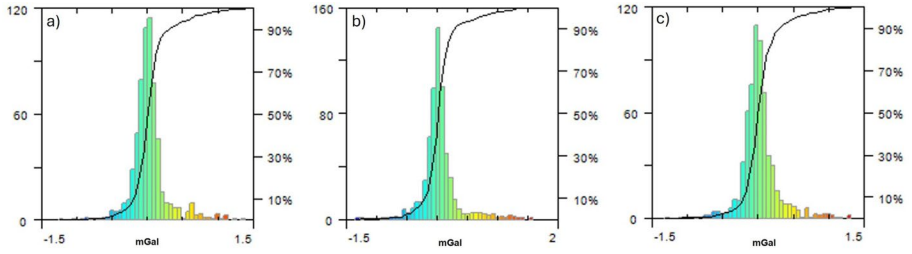


Fig. 8 Misfit histograms of the inversion of gravity data in the LHGF using the geological model of Calcagno et al. (2022) with input density values of C2 for the probability of property changes of (a) 60% of density changes and 40% of changes in the structural model, (b) 80% of density changes and 20% of changes in the structural model, and (c) 70% of density changes and 30% of changes in the structural model

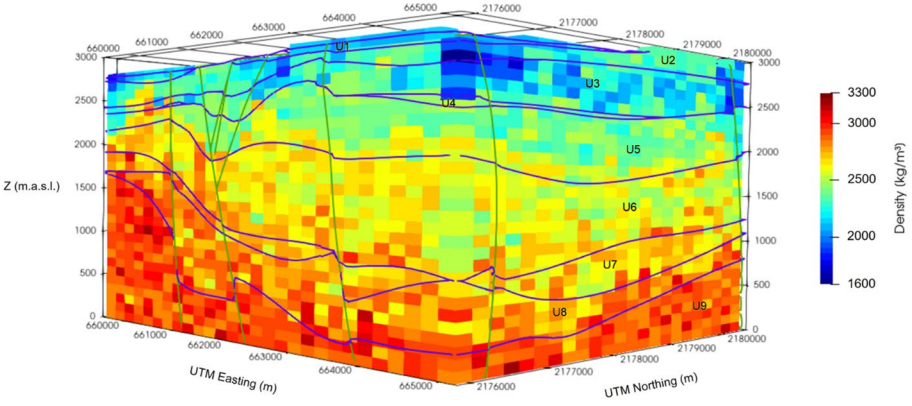


Fig. 9 The 3-D density distribution derived from inverse modeling using 70% probability for density changes and 30% for geometry changes, constrained by the local 3-D geological model(Calcagno et al. 2022) and the C2 initial density distribution. The purple and green lines represent the boundaries of the geological units and faults of Calcagno et al. 2022 model, respectively

Material). Units 6 to 9 display nearly symmetrical density distributions, with skewness values below 0.1, suggesting more homogeneous rock characteristics in these units.

To quantify which parts of the model contributed most to the improvement of the gravity fit, Fig. 11 shows the density increase retrieved by the inversion for each geological unit ($\Delta\rho = \rho_{final} - \rho_{initial}$). The ρ_{final} corresponds to the mean density value obtained from the inversion gravity modeling. The largest increments, up to 120–130 kg/m^3, occur in units U1 and U4. Moderate increase in U5-U6 likely reflect local

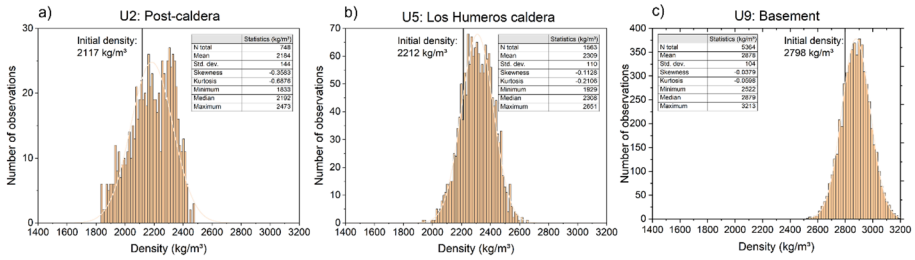


Fig. 10 Histograms of the density distributions of representative units **a**) Unit 2, Post-caldera deposits, **b**) Unit 5, Los Humeros caldera deposits, **c**) Unit 9, basement. The black vertical lines indicate the initial densities

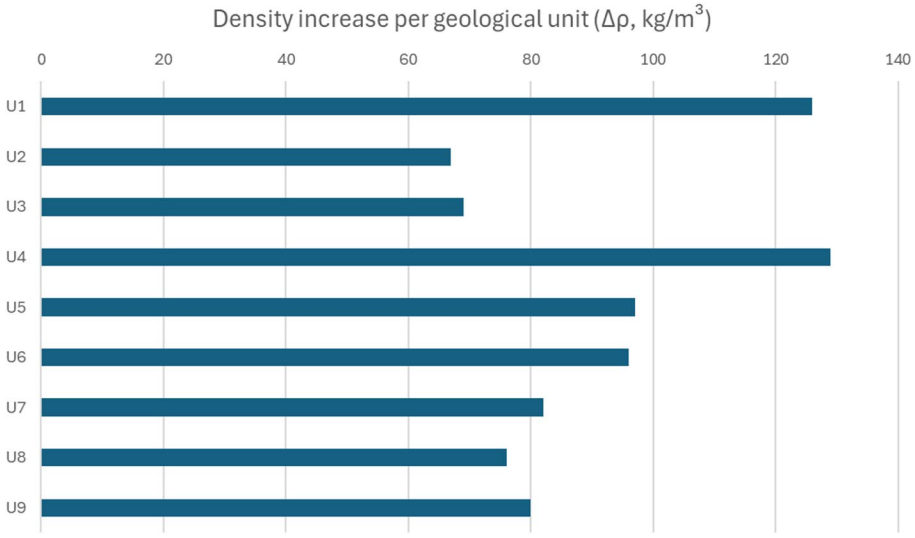


Fig. 11 Density increases per geological unit after inversion. The positive $\Delta\rho$ values indicate that input saturated mean bulk densities were consistently underestimated

adjustments within compacted volcanic units, while U7-U9 exhibit minor changes, consistent with their more homogeneous lithologies.

Discussion and conclusion

Typically, uncertainties in gravity analyses are attributed to instrumental and measurement errors, operator-related effects, environmental influences, and inaccuracies in data reduction or compiled datasets (e.g., Athens and Caers 2021). Our results extend beyond these common error sources by explicitly analyzing the effect of compaction and fluid saturation on the initial models, which directly influence bulk density distributions (Balza and Li 2020).

Our results highlight the limitations of 3-D gravity forward modeling in complex geothermal settings. Across all density-parameterization scenarios, the computed gravity exhibits a systematic negative shift relative to observed anomalies, with discrepancies on the order of several milligals (Fig. 5). This underestimation indicates that the models do not fully capture the true mass distribution, likely reflecting unmodeled contributions from the deeper subsurface. While more sophisticated parameterizations reduce misfit to some extent, the modeled values remain significantly divergent from the observations.

Analysis of the misfit distributions shows a progression from a left-skewed histogram in C1 toward a more Gaussian form in C2, suggesting partial improvement in

reproducing the gravity anomalies. Nonetheless, even in C2, considerable misfit persists, and although C3 shifts more cells toward lower misfit, it still fails to achieve an overall acceptable fit. These results underscore the challenges inherent to forward modeling gravity in geothermal reservoirs, where small-scale density variations and complex subsurface structures often produce signals that cannot be fully captured.

The inversion results primarily demonstrate the effectiveness of 3-D gravity inversion constrained by geological models in resolving subsurface density distributions. Using the 3-D geological framework of Calcagno et al. (2022) and initial density distributions (C1–C3), forward perturbation of each cell highlights the sensitivity of the gravity response to both density and structural variations. Allowing equal probabilities of change in densities and geological structures improved the fit to observed gravity, with the most substantial improvement observed for C2. The use of a multi-modal density approach (C3) in the inversion (Fig. 7) did not further reduce the misfit; instead, it increased the skewness toward higher density values. This likely reflects the challenge of capturing the high geological heterogeneity of the LHGF with a simplified statistical representation of lithological fractions, compounded by uneven availability of petrophysical data across units and the inherent uncertainties in both the geological model and gravity measurements. Similarly, despite extensive efforts in data acquisition, the initial density values systematically underestimated the optimal densities determined by inversion by approximately 60–130 kg/m^3, with large variations across different lithologies.

Misfit histograms show that modest perturbations reduce skewness but retain some negative bias, whereas increasing the number of perturbations to 40 per cell enables convergence toward a Gaussian misfit distribution with a half-width of ± 0.2 mGal. This demonstrates the importance of sufficient sampling of model uncertainty, particularly in complex, heterogeneous geothermal systems.

Analysis of the relative contribution of density versus structural adjustments (Table 2; Fig. 8) reveals that prioritizing density changes over structural modifications yields the best overall fit. Specifically, the scenario with 70% probability for density changes and 30% for structural adjustments produced the lowest standard deviation in misfit, low skewness, and acceptable kurtosis. These findings underscore that, for geothermal reservoirs, density variations—driven by compaction, porosity, and fluid saturation—play a dominant role in shaping the gravity response, whereas structural refinements have a secondary effect.Compared with earlier 3-D gravity inversions in geothermal systems (e.g., Witter et al. 2016; Guillen et al. 2008), this study advances the methodology in both the definition and treatment of density parameters. Witter et al. (2016) successfully introduced heterogeneous starting densities constrained by a 3-D geological model; however, the densities were estimated rather than validated by laboratory measurements, and in-situ effects such as compaction and saturation were not considered. Here, we complement that approach by integrating a measured petrophysical database corrected for depth-dependent porosity and fluid conditions, and by applying a probabilistic inversion framework that jointly explores density and geometric uncertainty. This strategy allows for a physically consistent parameterization of each lithological unit and provides a quantitative basis for assessing model reliability.

Regarding the sensitivity of the inversion results with respect to depth, it was evaluated by extending the model domain from the surface down to 7,000 m b.s.l., matching the base of the 3-D geological model. The resulting density patters and misfit values

changes only marginally below roughly 3,000 m, indicating that the gravity field primarily reflects density contrasts within the shallow and intermediate geological units. Consequently, the final model was limited to 0 m a.s.l., which approximately corresponds to the maximum depth of the basement roof in the inversion area. These results confirm that the gravity data provide meaningful resolution above this dept, whereas density variations at greater depths have a negligible influence on the observed field.

Geologically, density variations are smaller within the pre-caldera units, suggesting more homogeneous rock properties. The greatest heterogeneity in rock properties and lithologies is observed in the upper model units. These units contain small-scale lava flows and highly porous fall-out deposits. A portion of the observed density variability may be attributed to the presence of fault zones, which locally alter the subsurface structure and porosity. Small magmatic intrusions at shallow depths within the Los Potreros caldera, acting as local heat sources, may also account for the observed density variability (Deb et al. 2021; Lucci et al. 2020; Urbani et al. 2020). Additionally, distinguishing between welded (very low porosity) and unwelded tuffs or ignimbrites within Unit 5 is particularly challenging, as these variations can occur over distances of just tens of meters. For Units 3 and 4, data is either entirely lacking or extremely limited.

Analysis of the density distributions obtained from the inversion provides important insights into the internal heterogeneity of the LHGF. The upper volcanic units (U1–U5) exhibit predominantly log-normal distributions, indicating that most voxels correspond to lower-density volcanic rocks, while a smaller fraction reaches higher densities due to localized compaction, welding, or hydrothermal alteration. In contrast, the deeper pre-caldera and basement units (U6–U9) display nearly symmetrical (Gaussian) distributions with skewness below 0.1, reflecting a much greater internal homogeneity. These deeper units correspond to dense basalts, andesites, skarns, and marbles, which are less affected by alteration and faulting.

The transition from highly variable densities in the upper units to uniform densities in the basement highlights the lithological and structural hierarchy of the system, with heterogeneity concentrated near the surface and increasing consolidation at depth. This vertical trend suggests that density contrasts in the LHGF primarily arise from near-surface lithological variability and structural disruption rather than deeper thermal or fluid effects. Unlike studies in non-volcanic settings, where gravity lows have indicated fractured geothermal reservoirs (e.g., Altwegg et al. 2015), our gravity modeling primarily reflects geological structure rather than directly delineating the reservoir.

Finally, given the large lithological variability of the LHGF, where volcanic and sedimentary rocks coexist within the reservoir sequence, we adopted a general empirical approach that incorporate P-wave and S-wave velocity data into the compaction correction. Nevertheless, to improve the density-depth correction, new high-temperature and high-pressure experiments would be required to determine site-specific correction functions for the different lithologies present at Los Humeros.

In conclusion, our approach reveals a method to semi-quantify the uncertainty of geological models. By incorporating variable probabilities for density and geometry changes, we were able to assess how well the initial geological model aligns with observed data and where adjustments are most effective. Our approach not only improves gravity modeling outcomes but also provides a framework for assessing the reliability and limitations of geological interpretations in complex geothermal settings.

Supplementary Information

The online version contains supplementary material available at https://doi.org/10.1186/s40517-026-00395-4.

Supplementary Material 1.

Acknowledgements

This work was carried out in the framework of the GEMex project, which received funding from the European Union's EU Horizon 2020 research and innovation program under grant agreement No. 727550 and the Mexican government under grant agreement No. 268074 (http://www.gemex-h2020.eu). Eva Schill and Natalia Cornejo acknowledge funding through the program Materials and Technologies for the Energy Transition (MTET) of the Helmholtz Association. In addition, Eva Schill acknowledges the support by the U.S. Department of Energy, Office of Energy Efficiency and Renewable Energy (EERE), Geothermal Technologies Office, under Award Number DE-AC02–05CH11231 with Lawrence Berkeley National Laboratory.

Author contributions

NCT: acquisition, processing, and modeling of the local gravity data, analysis of the regional gravity data, writing. LMW: density parametrizations, writing and editing. ES: concept of the study, writing, review and editing and IS: review and editing. All authors read and approved the final manuscript.

Funding

This work was carried out in the framework of the GEMex project, which received funding from the European Union's EU Horizon 2020 research and innovation program under grant agreement No. 727550 and the Mexican government under grant agreement No. 268074 (http://www.gemex-h2020.eu). Eva Schill and Natalia Cornejo acknowledge funding through the program Materials and Technologies for the Energy Transition (MTET) of the Helmholtz Association. In addition, Eva Schill acknowledges the support by the U.S. Department of Energy, now Hydrocarbon and Geothermal Energy Office (HGEO), under Award Number DE-AC02–05CH11231 with Lawrence Berkeley National Laboratory.

Data availability

The datasets generated and analyzed during the current study within the framework of the GEMex project are available in the GEMex Open Access DB repository (https://gemex.igg.cnr.it/). The gravity data that support the findings of this study at regional scale were kindly provided by the Comisión Nacional de Hidrocarburos (http://www.gob.mx/cnh), but restrictions apply to the availability of these data, which were used under license for the current study, and so are not publicly available.

Declarations

Competing interests

The authors declare no competing interests.

Received: 4 September 2025 / Accepted: 23 June 2026

Published online: 03 July 2026

References

Agnew DC. SPOTL: Some Programs for Ocean-Tide Loading (Report). La Jolla, CA: Scripps Institution of Oceanography; 2012.

Altwegg P, Schill E, Abdelfettah Y, Radogna PV, Mauri G. Toward fracture porosity assessment by gravity forward modeling for geothermal exploration (Sankt Gallen, Switzerland). Geothermics. 2015;57:26–38. https://doi.org/10.1016/j.geothermics.2015.05.006.

Ashena R, Behrenbruch P, Ghalambor A. Log-based rock compressibility estimation for Asmari carbonate formation. J Petroleum Explor Prod Technol. 2020;10(7):2771–83. https://doi.org/10.1007/s13202-020-00934-0.

Athens ND, Caers JK. Gravity inversion for geothermal exploration with uncertainty quantification. Geothermics. 2021;97:102230. https://doi.org/10.1016/j.geothermics.2021.102230.

Athy LF. Density, Porosity, and Compaction of Sedimentary Rocks. AAPG Bull. 1930;14. https://doi.org/10.1306/3D93289E-16B1-11D7-8645000102C1865D.

Baillieux P, Schill E, Edel JB, Mauri G. Localization of temperature anomalies in the Upper Rhine Graben: Insights from geophysics and neotectonic activity. Int Geol Rev. 2013;55(14):1744–62. https://doi.org/10.1080/00206814.2013.794914.

Baillieux P, Schill E, Abdelfettah Y, Dezayes C. (2014). Possible natural fluid pathways from gravity pseudo-tomography in the geothermal fields of Northern Alsace (Upper Rhine Graben). www.geothermal-energy-journal.com/content/2/1/16

Balza A, Li Y. Integrating time-lapse gravity, production, and geologic structure data in a gas reservoir study. Interpretation. 2020;8(4). https://doi.org/10.1190/INT-2019-0272.1. .SS129-SS143.

Bernard R, Taran Y, Pennisi M, Tello E, Ramirez A. Chloride and Boron behavior in fluids of Los Humeros geothermal field (Mexico): A model based on the existence of deep acid brine. Appl Geochem. 2011;26(12):2064–73. https://doi.org/10.1016/j.apgeochem.2011.07.004.

Calcagno P, Chilès JP, Courrioux G, Guillen A. Geological modelling from field data and geological knowledge. Part I. Modelling method coupling 3D potential-field interpolation and geological rules. Phys Earth Planet Inter. 2008;171(1–4):147–57. https://doi.org/10.1016/j.pepi.2008.06.013.

Calcagno P, Evanno G, Trumpy E, Carlos Gutiérrez-Negrín L, Maclás JL, Carrasco-Núñez G, Liotta D. Preliminary 3-D geological models of Los Humeros and Acoculco geothermal fields (Mexico)-H2020 GEMex Project. Adv Geosci. 2018;45:321–33. https://doi.org/10.5194/adgeo-45-321-2018.

Calcagno P, Trumpy E, Gutiérrez-Negrín LC, Liotta D. A collection of 3D geomodels of the Los Humeros and Acoculco geothermal systems (Mexico). Sci Data. 2022;9(1). https://doi.org/10.1038/s41597-022-01327-0.
Carrasco-Núñez G, McCurry M, Branney MJ, Norry M, Willcox C. Complex magma mixing, mingling, and withdrawal associated with an intra-Plinian ignimbrite eruption at a large silicic caldera volcano: Los Humeros of central Mexico. Bull Geol Soc Am. 2012;124(11–12):1793–809. https://doi.org/10.1130/B30501.1.
Carrasco-Núñez G, Hernández J, De Léon L, Dávilla PNG, Bernal JP, Jicha B, Jicha B, Navarro M, López-Quiroz P. Geologic Map of Los Humeros volcanic complex and geothermal field eastern Trans-Mexican Volcanic Belt. Terra Digitalis. 2017a;1:1–11. https://doi.org/10.22201/igg.terradigitalis.2017.2.24.78.
Carrasco-Núñez G, López-Martínez M, Hernández J, Vargas V. Subsurface stratigraphy and its correlation with the surficial geology at Los Humeros geothermal field, eastern Trans-Mexican Volcanic Belt. Geothermics. 2017b;67:1–17. https://doi.org/10.1016/j.geothermics.2017.01.001.
Carrasco-Núñez G, Bernal JP, Dávila P, Jicha B, Giordano G, Hernández J. Reappraisal of Los Humeros Volcanic Complex by New U/Th Zircon and 40Ar/39Ar Dating: Implications for Greater Geothermal Potential. Geochem Geophys Geosyst. 2018;19(1):132–49. https://doi.org/10.1002/2017GC007044.
Carrasco-Núñez G, Cavazos-Álvarez J, Dávila-Harris P, Bonini M, Giordano G, Corbo-Camargo F, Hernández J, López P, Lucci F. Assembly and development of large active calderas hosting geothermal systems: Insights from Los Humeros volcanic complex (Mexico). J S Am Earth Sci. 2022;120. https://doi.org/10.1016/j.jsames.2022.104056.
Cattin R, Mazzotti S, Baratin LM. Comput Geosci. 2015;81:20–7. https://doi.org/10.1016/j.cageo.2015.04.005. GravProcess: An easy-to-use MATLAB software to process campaign gravity data and evaluate the associated uncertainties.
Cavazos-Álvarez JA, Carrasco-Núñez G, Dávila-Harris P, Peña D, Jáquez A, Arteaga D. Facies variations and permeability of ignimbrites in active geothermal systems; case study of the Xáltipan ignimbrite at Los Humeros Volcanic Complex. J S Am Earth Sci. 2020;104:102810. https://doi.org/10.1016/j.jsames.2020.102810.
Cornejo-Triviño N, Liotta D, Piccardi L, Brogi A, Kruszewski M, Perez-Flores MA, Carrillo J, Calcagno P, Sass I, Schill E. Gravimetric and morpho-structural analyses in the superhot geothermal system Los Humeros: an example from central Mexico. Geotherm Energy. 2024;12(1). https://doi.org/10.1186/s40517-024-00285-7.
Deb P, Giordano G, Shi X, Lucci F, Clauser C. An approach to reconstruct the thermal history in active magmatic systems: Implications for the Los Humeros volcanic complex, Mexico. Geothermics. 2021;96. https://doi.org/10.1016/j.geothermics.2021.102162.
Ferriz H, Mahood GA. Eruption rates and compositional trends at Los Humeros volcanic center, Puebla, Mexico. J Phys Res. 1984;89(B10):8511–24. https://doi.org/10.1029/JB089iB10p08511.
Guglielmetti L, Comina C, Abdelfettah Y, Schill E, Mandrone G. Integration of 3D geological modeling and gravity surveys for geothermal prospection in an Alpine region. Tectonophysics. 2013;608:1025–36. https://doi.org/10.1016/j.tecto.2013.07.012.
Guillen A, Calcagno P, Courrioux G, Joly A, Ledru P. Phys Earth Planet Inter. 2008;171(1–4):158–69. https://doi.org/10.1016/j.pepi.2008.06.014. Geological modelling from field data and geological knowledge. Part II. Modelling validation using gravity and magnetic data inversion.
Holstein H. Gravimagnetic anomaly formulas for polyhedra of spatially linear media. Geophysics. 2003;68(1):157–67. https://doi.org/10.1190/1.1543203.
Kane MF. A comprehensive system of terrain corrections using a digital computer. Geophysics. 1962;27(4):455–62. https://doi.org/10.1190/1.1439044.
Lafehr TR. (1991). An exact solution for the gravity curvature (Bullard B) correction. In GEOPHYSICS (56, Issue 8). http://library.seg.org/
Lucci F, Carrasco-Núñez G, Rossetti F, Theye T, White C, Urbani J, Azizi S, Asahara H, Y., Giordano G. Anatomy of the magmatic plumbing system of Los Humeros Caldera (Mexico): Implications for geothermal systems. Solid Earth. 2020;11(1):125–59. https://doi.org/10.5194/se-11-125-2020.
Nagy D. The prism method for terrain corrections using digital computers. Pure appl Geophys. 1966;63(1):31–9. https://doi.org/10.1007/BF00875156.
Norini G, Carrasco-Núñez G, Corbo-Camargo F, Lermo J, Rojas JH, Castro C, Bonini M, Montanari D, Corti G, Moratti G, Piccardi L, Chavez G, Zuluaga MC, Ramirez M, Cedillo F. The structural architecture of the Los Humeros volcanic complex and geothermal field. J Volcanol Geoth Res. 2019;381:312–29. https://doi.org/10.1016/j.jvolgeores.2019.06.010.
Okabe M. Analytical expressions for gravity anomalies due to homogeneous polyhedral bodies and translations into magnetic anomalies. Geophysics. 1979;44(4):730–41. https://doi.org/10.1190/1.1440973.
Pinti DL, Castro MC, López-Hernández A, Hernández-Hernández MA, Shouakar-Stash O, Hall CM, Bahena-Romero J, Ramírez-Montes M. Origin of volatile species and aqueous fluids in the Los Humeros Geothermal Field, Mexico. Chem Geol. 2021;584:120539. https://doi.org/10.1016/j.chemgeo.2021.120539.
Plouff D. Gravity and magnetic fields of polygonal prisms and application to magnetic terrain corrections. Geophysics. 1976;41(4):727–41. https://doi.org/10.1190/1.1440645.
Prol-Ledesma RM, Browne PRL. Hydrothermal alteration and fluid inclusion geothermometry of los humeros geothermal field. Mexico Geothermics. 1989;18(5–6):677–90. https://doi.org/10.1016/0375-6505(89)90100-4.
Agnew DC. Earth Tides. In: Schubert G, editor. Treatise on Geophysics. Elsevier Science; 2007. pp. 163–95.
Telford WM, Geldart LP, Sheriff RE. Applied Geophysics. 2nd ed. Cambridge University Press; 1990.
Tello HE. (2005). Estado de equilibrio soluto-mineral y saturación de minerales de alteración en fluidos geotérmicos de alta temperature. [Tesis doctoral, Universidad Autónoma de México]. https://tesiunamdocumentos.dgb.unam.mx/ptb2005/01190/0346539/0346539_A1.pdf
Urbani S, Giordano G, Lucci F, Rossetti F, Acocella V, Carrasco-Núñez G. Estimating the depth and evolution of intrusions at resurgent calderas: Los Humeros (Mexico). Solid Earth. 2020;11(2):527–45. https://doi.org/10.5194/se-11-527-2020.
Urbani S, Giordano G, Lucci F, Rossetti F, Carrasco-Núñez G. Reply to Norini and Groppelli's comment on Estimating the depth and evolution of intrusions at resurgent calderas: Los Humeros (Mexico) by Urbani et al. (2020). Solid Earth. 2021;12(5):1111–24. https://doi.org/10.5194/se-12-1111-2021.
Weydt LM, Bär K, Sass I. Petrophysical characterization of the Los Humeros geothermal field (Mexico): from outcrop to parametrization of a 3D geological model. Geotherm Energy. 2022a;10(1). https://doi.org/10.1186/s40517-022-00212-8.

Weydt LM, Ramírez-Guzmán ÁA, Pola A, Lepillier B, Kummerow J, Mandrone G, Comina C, Deb P, Norini G, Gonzalez-Partida E, Ramón Avellán D, Maciás JL, Bär K, Sass I. Petrophysical and mechanical rock property database of the Los Humeros and Acoculco geothermal fields (Mexico). Earth Syst Sci Data. 2021;13(2):571–98. https://doi.org/10.5194/essd-13-571-2021.

Weydt LM, Lucci F, Lacinska A, Scheuvens D, Carrasco-Núñez G, Giordano G, Rochelle CA, Schmidt S, Bär K, Sass I. The impact of hydrothermal alteration on the physiochemical characteristics of reservoir rocks: the case of the Los Humeros geothermal field (Mexico). Geotherm Energy. 2022b;10(1):20. https://doi.org/10.1186/s40517-022-00231-5.

Willcox CP. (2012). Eruptive, Magmatic and Structural Evolution of a Large Explosive Caldera Volcano: Los Humeros, Central Mexico [PhD thesis]. University of Leicester.

Witter JB, Siler DL, Faulds JE, Hinz NH. Nev USA Geotherm Energy. 2016;4(1). https://doi.org/10.1186/s40517-016-0056-6. 3D geophysical inversion modeling of gravity data to test the 3D geologic model of the Bradys geothermal area.

Yáñez-García C, García-Durán S. Exploración de la región geotérmica Los Humeros-Las Derrumbadas, estados de Puebla y Veracruz (Report). Mexico: Comision Federal de Electricidad; 1982.

Zhu Z, Tian H, Jiang G, Dou B. (2022). Effects of high temperature on rock bulk density. In Geomechanics and Geoengineering (Vol. 17, Issue 2, pp. 647–657). Taylor and Francis Ltd. https://doi.org/10.1080/17486025.2020.1827169

Publisher's note

Springer Nature remains neutral with regard to jurisdictional claims in published maps and institutional affiliations.